Petroleum Science 23 (2026) 7296–7308

Contents lists available at ScienceDirect

Petroleum Science

journal homepage: www.keaipublishing.com/en/journals/petroleum-science

Original Paper

Erosion characteristics and energy economy of low-pressure abrasive gas jet across distinct lithologies

Jing-Ru Hu [a,b], Dong Yang [a,b], Shi-Hao Zhang [a,b], Pei-Sen Li [a,b], Long-Hao Zhao [a,b], Jing-Bin Li [a,b,*], Huan Li [a,b], Hou Zhong [a,b], Zhong-Wei Huang [a,b]

[a] State Key Laboratory of Petroleum Resources and Engineering, China University of Petroleum (Beijing), Beijing, 102249, China
[b] College of Petroleum Engineering, China University of Petroleum (Beijing), Beijing, 102249, China

ARTICLE INFO

Article history:
Received 28 December 2025
Received in revised form
5 March 2026
Accepted 15 June 2026
Available online 20 June 2026

Edited by Xi Zhang

Keywords:
Abrasive gas jet
Hard rock breakage
Specific energy
Laval nozzle
Erosion mechanism

ABSTRACT

The exploitation of deep-earth energy resources demands rock excavation technologies that are efficient, compact, and reservoir-friendly. While high-pressure abrasive water jets (HPAWJ) are effective, they suffer from heavy logistical burdens and potential formation damage. This study investigates the feasibility and energy economy of an abrasive gas jet (AGJ) system driven by a Laval nozzle to break hard rocks using standard industrial low-pressure air (<0.6 MPa). Systematic experiments were conducted on sandstone, limestone, and granite to determine critical breaking pressure thresholds and characterize the evolution of hole depth, diameter, and volumetric removal under varying jet pressures and exposure times. The results quantify distinct thresholds of ≤0.05 MPa for sandstone, 0.15 MPa for limestone, and 0.25 MPa for granite, confirming that dynamic tensile fracture enables hard rock erosion without ultra-high-pressure intensification. Lithology-dependent erosion kinetics were elucidated: sandstone exhibits a non-linear saturation trend due to the debris cushioning effect; limestone maintains stable linear growth via lamellar spalling; while granite is dominated by brittle chipping but faces deceleration in deep cavities due to geometric confinement. In terms of energy economy, based on the rigorous adiabatic compression work model, the AGJ system achieves a specific energy of 4.43×10^{10} J/m^3 for fracturing granite at 0.25 MPa. This represents an energy cost reduction of approximately 39% compared to submerged abrasive water jets operating at 25 MPa, demonstrating that high-velocity compressible flow can match hydraulic breaking efficiency at 1/100th of the driving pressure. These findings establish a thermodynamic justification for utilizing low-pressure AGJ and propose lithology-specific operational strategies for subsurface energy engineering.
© 2026 The Authors. Publishing services by Elsevier B.V. on behalf of KeAi Communications Co. Ltd. This is an open access article under the CC BY-NC-ND license (http://creativecommons.org/licenses/by-nc-nd/4.0/).

1. Introduction

The global transition toward deep-earth energy utilization has imposed stringent requirements on rock excavation technologies (Gao et al., 2022; Li et al., 2022). Whether for deep geothermal exploitation, underground gas storage (UGS) construction, or CO_2 geological sequestration, the engineering objective has shifted from simple volume removal to efficient, compact, and reservoir-adaptable excavation (Song and Zhang, 2013; Zhang and Zhao, 2019; Liu et al., 2020a; Ehlig-Economides, 2023). In these subsurface campaigns, engineers encounter a diverse geological spectrum, ranging from weak sedimentary deposits to high-strength, abrasive crystalline basements (Sun et al., 2024). While mechanical cutting remains the industry standard, its limitations are prohibitive: rapid tool wear in hard strata drives up operational costs, and the heavy, bulky machinery lacks the flexibility required for confined, geometrically restricted underground spaces (Zhao et al., 2019; Deng et al., 2022; Hamzaban et al., 2023; Fu et al., 2025).

To transcend these mechanical limits, fluid-assisted technologies have been extensively deployed. HPAWJ have proven effective in fracturing competent rock (Lu et al., 2019; Ge et al., 2023; Wang et al., 2023). However, their reliance on massive hydraulic systems imposes a heavy logistical burden, and the introduction of aqueous fluids poses risks to water-sensitive reservoirs through clay

* Corresponding author.
E-mail address: lijb@cup.edu.cn (J.-B. Li).
Peer review under the responsibility of China University of Petroleum (Beijing).

https://doi.org/10.1016/j.petsci.2026.06.028
1995-8226/© 2026 The Authors. Publishing services by Elsevier B.V. on behalf of KeAi Communications Co. Ltd. This is an open access article under the CC BY-NC-ND license (http://creativecommons.org/licenses/by-nc-nd/4.0/).

swelling and permeability impairment (Wang et al., 2018; Li et al., 2025b). Emerging alternatives, such as supercritical CO_2 jet technology (Wang et al., 2015; He et al., 2016; Huang et al., 2020), offer a waterless solution but are currently hindered by high system complexity, phase state instability, and the excessive cost of maintaining conditions in field environments (Ren et al., 2025; Xi et al., 2025). Consequently, the industry faces an urgent demand for a rock breakage technology that is structurally compact, functionally anhydrous, and simpler to deploy than supercritical systems.

An abrasive gas jet (AGJ) offers a compelling solution to these operational bottlenecks. By substituting liquid carriers with a high-velocity gas stream, AGJ eliminates the need for hydraulic pumps and fluid recycling units, offering a lightweight, non-contact erosion mechanism (Liu et al., 2020b). This technology has achieved industrial success in the coal sector for slotting and permeability enhancement (Liu et al., 2017, 2018). However, these applications have largely been restricted to soft coal seams (Ranjith et al., 2019; Hong et al., 2021). Extending AGJ to competent hard rock represents a significant technical frontier.

Previous experimental studies have demonstrated the feasibility of cutting hard rocks (e.g., granite) using AGJ driven by convergent-divergent Laval nozzles (Liu et al., 2020c). However, a critical gap exists between these laboratory successes and field applicability. Most effective hard-rock erosion tests rely on pre-pressurized gas cylinders to supply jet pressure exceeding 2 MPa (Hu et al., 2026; Wei et al., 2025). While these studies confirm that Laval nozzles can accelerate abrasive particles to erosive velocities at high inlet pressures, gas cylinders are inherently constrained by finite volumetric capacity and cannot support the continuous, high-flux operation required for industrial excavation. Conversely, standard industrial screw compressors, which supply the continuous air flow necessary for engineering scale, are typically rated for much lower pressures.

This dichotomy presents a fundamental engineering challenge: can the kinetic energy required for hard rock failure be maintained using the continuous, low-pressure supply of standard industrial compressors, rather than the high-pressure, discontinuous supply of gas cylinders? Although the aerodynamic principles of Laval nozzles have been well-established (Achtsnick et al., 2005; Hu et al., 2025), their efficacy in the ultra-low pressure regime (<0.6 MPa) for hard rock breakage remains under-explored. If the aerodynamic efficiency can be sufficiently optimized to break granite at such low jet pressures, it would bridge the gap between laboratory feasibility and industrial scalability, enabling continuous hard rock excavation using ubiquitous industrial air sources.

In this study, an integrated AGJ system driven by a Laval nozzle was developed to operate at extremely low jet pressures (<0.6 MPa), utilizing a continuous compressor source to simulate realistic field conditions. Using garnet as the abrasive medium, systematic experiments were conducted on three representative lithologies: sandstone, limestone, and granite. The study focuses on quantifying the critical breaking thresholds and examining the hole-forming characteristics under varying jet pressures and exposure times. Finally, a comparative energy analysis is performed to benchmark the efficiency of this low-pressure gas system, providing a theoretical and practical foundation for developing lightweight, continuous, and energy-efficient rock removal techniques for subsurface energy engineering.

2. Experimental setup and methods

2.1. Experimental apparatus

The experiments were performed using a custom-built AGJ system (Fig. 1), to ensure operational precision and safety, the apparatus is structurally organized into three distinct modules: a pneumatic supply unit, an abrasive feeding assembly, and a jetting and environmental control system.

Compressed air is generated by an industrial screw compressor and subsequently buffered in a surge tank. This buffering stage mitigates pressure pulsations from the compressor, ensuring stable isobaric conditions throughout the pipeline. Downstream of the tank, a pressure regulating valve precisely adjusts the jet pressure, while the gas volumetric flow rate is monitored in real-time by a digital vortex flowmeter prior to entering the mixing stage.

The solid phase is managed by a pressurized abrasive hopper sealed with a flanged lid to maintain system integrity. The particle feed rate is governed by a rotary disc feeder driven by an external control unit. The pneumatic line connects to the upper port of the feeder housing; as the disc rotates, the high-velocity airflow traverses the aligned grid cells, purging the entrained abrasives vertically through the bottom outlet. This mechanism ensures the formation of a continuous, uniform gas-solid two-phase flow without mechanical blockage.

The two-phase mixture is directed into the jetting module and accelerated through a convergent-divergent Laval nozzle to impinge perpendicularly onto the rock specimen. The entire erosion process occurs within a fully enclosed jetting cabinet. The cabinet is equipped with optical viewports for visual monitoring and is coupled to a negative-pressure dust extraction system. This setup effectively contains the rebound particles and filters airborne dust, while the spent abrasives are collected via gravitational sedimentation at the cabinet base.

2.2. Materials

2.2.1. Rock samples

To comprehensively evaluate the rock-breaking performance of the AGJ system across a broad spectrum of geological competencies, three representative lithologies were selected, ranging from porous sedimentary reservoirs to hard crystalline basements.

Sandstone was chosen to represent relatively soft, clastic reservoir formations. It is characterized by a granular structure with distinct porosity and lower mechanical strength, making it susceptible to matrix detachment (Huang et al., 2017). Limestone represents medium-strength carbonate formations. Composed primarily of calcite, it exhibits a dense, homogeneous structure that typically fails via shear or tensile delamination (Porcarelli et al., 2021). Granite, a coarse-grained crystalline rock rich in quartz and feldspar, was included to assess the system's capability in high-strength, heterogeneous hard rock formations (Ait Baha et al., 2025).

All rock specimens were precision-cut into cubic blocks with dimensions of $200 \times 200 \times 200$ mm^3. This specific geometry was selected to ensure the target acts as a semi-infinite medium relative to the jet diameter, thereby effectively eliminating boundary reflection effects during jet impingement. The key physico-mechanical properties of these samples were determined via standard rock mechanics testing (ISRM standards) and are summarized in Table 1 (Ulusay, 2015).

2.2.2. Abrasive

In this study, commercial-grade garnet sand sourced from Henan, China, was employed as the abrasive medium due to its

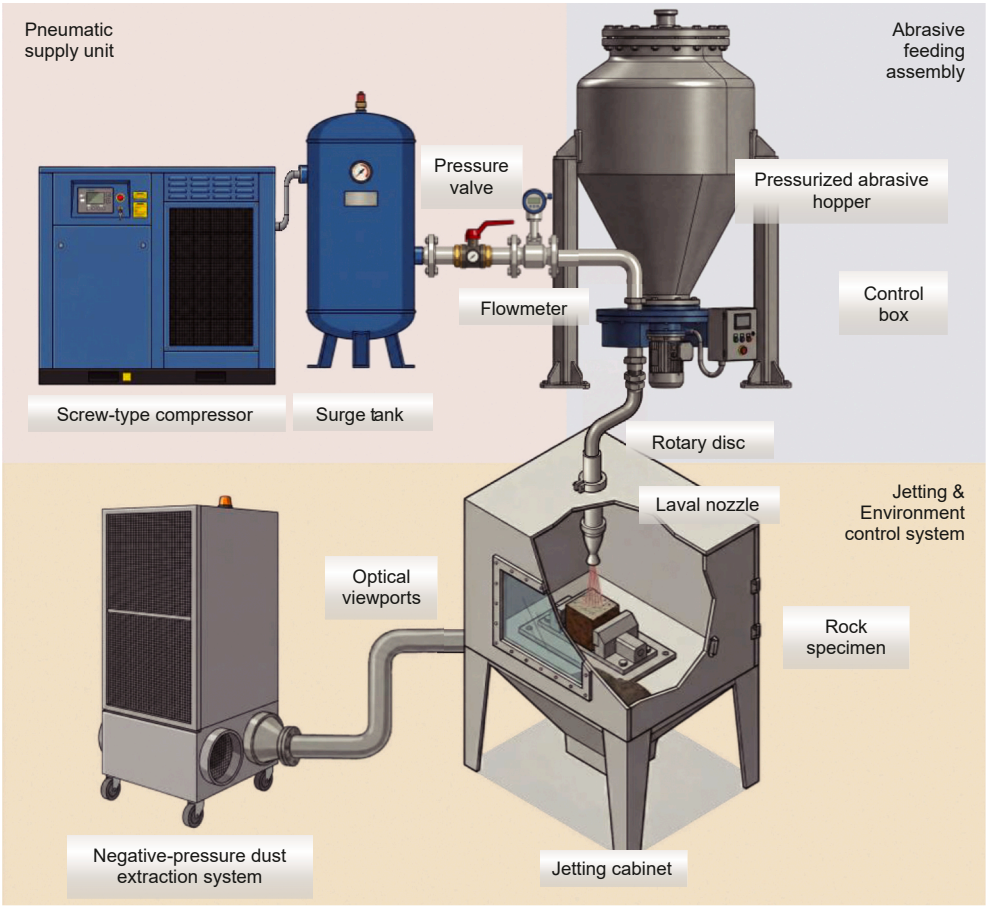


Fig. 1. Schematic diagram of the experimental abrasive gas jet (AGJ) system.

Table 1
Mechanical properties of the tested rock samples.

Rock type	Parameter	Value
Sandstone	Uniaxial compressive strength (σ_c), MPa	78.86
	Tensile strength (σ_t), MPa	3.16
	Shear strength (τ), MPa	5.72
Limestone	Uniaxial compressive strength (σ_c), MPa	95.92
	Tensile strength (σ_t), MPa	4.97
	Shear strength, (τ) MPa	10.03
Granite	Uniaxial compressive strength (σ_c), MPa	160.64
	Tensile strength (σ_t), MPa	6.42
	Shear strength (τ), MPa	10.50

superior hardness and chemical stability (Joo et al., 2023; Li et al., 2023). The morphological characteristics of the particles are visualized in Fig. 2. The macroscopic appearance (Fig. 2(a)) displays a consistent granular texture, while the microscopic morphology, captured via scanning electron microscopy (SEM) in Fig. 2(b), reveals distinct sharp edges and irregular geometries.

To quantitatively assess particle irregularity, a critical parameter governing erosion efficiency, representative grains were analyzed using ImageJ software. The shape factor (ϕ), often referred to as circularity, was calculated based on the formulation proposed by Cox (1927):

$$\phi = \frac{4\pi A}{{L_p}^2} \tag{1}$$

where A represents the two-dimensional projected area of the particle grain, L_p denotes the perimeter of the particle's projection boundary.

Theoretically, a shape factor of $\phi = 1.0$ corresponds to a perfect circle, while lower values indicate increasing angularity. For the garnet particles used in this campaign, the calculated average shape factor is 0.786. This deviation from circularity confirms the high angularity observed in the SEM micrographs, which is mechanically advantageous for enhancing the micro-cutting and plowing actions upon high-velocity impact with the rock surface (Li et al., 2025a). The key physical properties of the abrasive are summarized in Table 2.

2.2.3. Nozzle

A linear Laval nozzle (Fig. 3) was employed to accelerate the gas-solid two-phase flow to supersonic velocities. Fabricated from wear-resistant alloy steel to withstand abrasive erosion, the nozzle features a classic converging-diverging geometry with a conical divergent section. The critical geometric parameters include a throat diameter (D^*) of 8 mm and a design pressure ratio of 0.5 (Liu et al., 2020c). This specific geometric configuration is aerodynamically optimized for a design stagnation pressure of 0.55 MPa. At this maximum operating pressure, the nozzle is designed to achieve optimal expansion (Hu et al., 2025). While the experimental investigation covers a broad range (0.05–0.55 MPa), implying that the system operates in an over-expanded regime at lower pressures, this fixed geometry was strategically selected to prioritize jet stability and maximize kinetic energy transfer at the upper limit of the test spectrum.

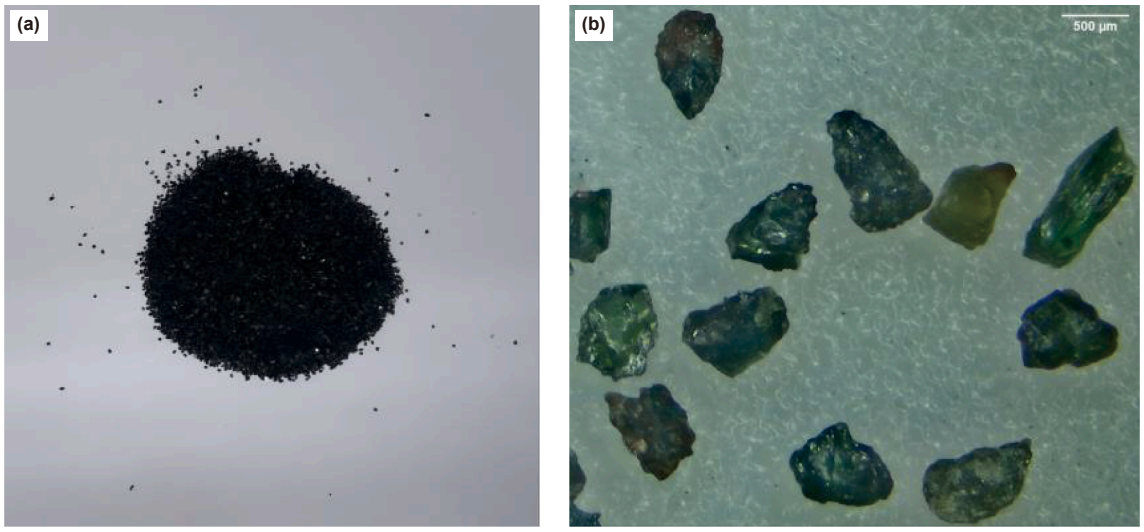


Fig. 2. Morphology of the garnet abrasive: (**a**) macroscopic photograph of the particle accumulation, (**b**) microscopic SEM image showing sharp angular edges.

Table 2
Physical properties of the garnet abrasive.

Property	Value
Density, kg/m^3	3784
Mohs hardness	8.0
Shape factor	0.786
Nominal particle size, mesh	46
Unit price, CNY/kg	2.5

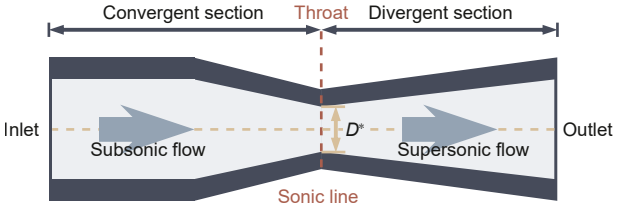


Fig. 3. Schematic cross-section of the Laval nozzle geometry showing key design parameters.

2.3. Experimental procedure

The experimental campaign was conducted using a vertical fixed-point jetting configuration. The jet pressure (P) is defined as the stagnation pressure measured at the nozzle inlet. To systematically quantify the rock-breaking thresholds and erosion kinetics, the testing program was executed in three phases (Table 3).

Scheme I (Threshold determination): An incremental pressurization method was adopted to identify the critical pressure required to initiate rock failure (P_{th}). The jet pressure was raised from 0.05 MPa in 0.05 MPa steps, with a short exposure duration of 5 s at each level. The breaking threshold was defined as the minimum pressure yielding a discernible macroscopic erosion volume ($V_e > 1000$ mm^3).

Scheme II & III (Parameter erosion experiments): Guided by the thresholds determined in Scheme I, parametric studies were conducted to evaluate the effects of jet pressure and exposure time. To ensure valid comparisons across lithologies with varying competencies, the starting pressure for these schemes was standardized to the maximum threshold ($P_{th,max}$). Scheme II investigated the pressure effect by varying P from $P_{th,max}$ up to the maximum stable system pressure of 0.55 MPa, while keeping the exposure time constant. Scheme III examined the temporal evolution by fixing P at 0.55 MPa and varying the jetting duration.

Throughout all tests, critical system parameters including nozzle standoff distance (S), impact angle (θ), and abrasive feed rate ($\dot{m}_a$) were maintained constant. Upon completion of each run, the erosion morphology was digitized using a high-precision 3D laser scanner (RigelScan Ultra, HEXAGON, Sweden) to extract the erosion depth (H_e), diameter (D_e), and volume (V_e). Each experimental condition was replicated three times to ensure statistical reliability.

3. Results

3.1. Breaking pressure thresholds

The breaking pressure threshold (P_{th}) serves as the critical determinant defining the lower operational boundary of the AGJ system. In this study, P_{th} is defined as the minimum jet pressure required to generate a macroscopic erosion volume exceeding 1000 mm^3 within a 5-s exposure. The evolution of removed volume with increasing jet pressure is presented in Fig. 4, revealing a distinct lithological hierarchy in erosion resistance.

The porous sandstone exhibited immediate susceptibility to the gas jet. Even at the minimum experimental pressure of 0.05 MPa, the erosion volume reached 2764.1 mm^3, far surpassing the failure criterion. This confirms that the threshold for this weakly cemented formation lies at or below 0.05 MPa, indicating its vulnerability to low-energy aerodynamic impact. In contrast, the limestone specimens displayed a step-wise activation behavior. Material removal remained negligible at 0.05 and 0.10 MPa, but a sharp volumetric surge to 1896.7 mm^3 occurred at 0.15 MPa, explicitly identifying this value as the effective breaking threshold for the carbonate formation.

The high-strength granite demonstrated the most significant resistance. In the sub-threshold regime (0.05–0.20 MPa), material removal was characterized by unstable superficial abrasion, with erosion volumes fluctuating stochastically between 300 mm^3 and 870 mm^3, consistently failing to meet the macroscopic breaking criterion. Effective fragmentation was achieved at 0.25 MPa, where the removal volume surpassed the threshold to reach 1142.3 mm^3.

Table 3
Experimental design and operating parameters of the AGJ system.

Category	Parameter	Value/Range
Fixed parameters	Standoff distance, mm	80
	Impact angle, °	90
	Abrasive feed rate, g/s	15
Schemes I: Threshold determination	Jet pressure, MPa	0.05– Incipient failure (Step: 0.05)
	Exposure time, s	5
Schemes II: Pressure effect	Jet pressure, MPa	$P_{th,max}$– 0.55
	Exposure time, s	30
Schemes III: Time effect	Jet pressure, MPa	0.55
	Exposure time, s	15/30/45/60/75

The granite threshold of 0.25 MPa carries direct engineering significance. This driving pressure is nearly three orders of magnitude below the compressive strength (σ_c = 160.64 MPa), confirming that the AGJ does not fracture rock through static pressurization of the gas phase. Instead, the Laval nozzle converts the modest inlet pressure into high-velocity particle impact, generating localized dynamic stresses that exceed the tensile strength of the rock — its weakest mechanical link. Since this threshold falls well within the rated capacity of standard industrial screw compressors (<1.2 MPa), the result validates the central hypothesis of this study: hard rock excavation can be achieved using continuous, low-pressure air sources without the need for high-pressure intensification equipment.

3.2. Evolution of erosion hole geometry

3.2.1. Morphological characteristics of erosion holes

To visualize the specific erosion patterns, the 3D surface topographies of the holes generated under the maximum impact energy condition (jet pressure of 0.55 MPa and exposure time of 75 s) were reconstructed. Fig. 5 presents the comparative morphologies of the three lithologies. While all specimens exhibit a general axisymmetric geometry, they display distinct topographic signatures regarding cross-sectional profiles and surface textures.

Sandstone (Fig. 5(a)–(d)) exhibits the most significant volumetric expansion, characterized by a broad, open U-shaped profile. The inner sidewalls display a uniform granular roughness, reflecting the detachment of discrete grains from the matrix. The crater bottom is wide and rounded, indicating that erosion propagated effectively in both lateral and vertical directions, resulting in a low aspect ratio cavity.

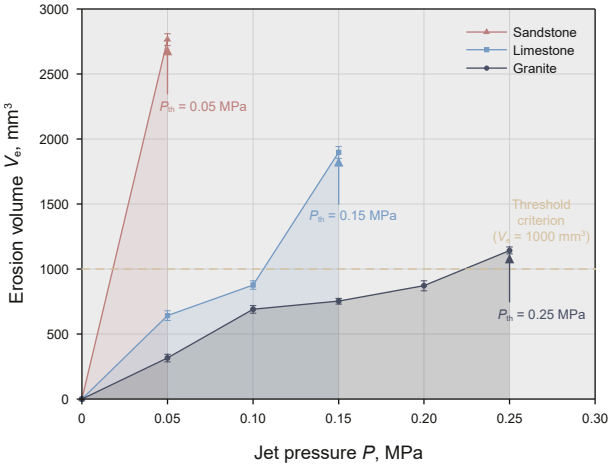


Fig. 4. Evolution of erosion volume (V_e) with jet pressure for the three lithologies, illustrating the determination of breaking pressure thresholds (P_{th}).

Limestone (Fig. 5(b)–(e)) presents a unique geometric signature distinguished by sidewall smoothness. Unlike the granular texture of sandstone, the limestone surface shows minimal macroscopic irregularities. A defining feature is the crater termination: the hole ends in a blunt, hemispherical bottom. The curvature remains consistent from the sidewall to the tip, suggesting a uniform material removal process.

Granite (Fig. 5(c)–(f)) stands in sharp contrast to the sedimentary rocks, featuring a strict V-shaped morphology. The inner walls are notably rugged, pitted, and stepped, rather than smooth. This surface is covered with irregular cavities and protrusions, reflecting the stochastic nature of brittle chipping. The hole terminates in a sharp, acute tip, indicating that the high-velocity energy was highly localized along the jet axis, creating a narrow, penetrating geometry.

3.2.2. Effect of jet pressure on erosion dimensions

The evolution of hole depth (H_e) and average diameter (D_e) was analyzed under a fixed exposure time of 30 s. As shown in Fig. 6, erosion dimensions exhibit a monotonic positive correlation with jet pressure across all lithologies. The results demonstrate a strict hierarchy in erosion magnitude: sandstone > limestone > granite, which correlates inversely with the geomechanical strength of the targets listed in Table 1. Specifically, at the maximum pressure of 0.55 MPa, the erosion depth in sandstone was approximately double that of granite, highlighting the dominant role of rock mechanical properties in resisting aerodynamic erosion.

Sandstone (Fig. 6(a)) exhibited the highest volumetric removal but the lowest relative sensitivity to pressure increments. As pressure rose from 0.25 to 0.55 MPa, the hole depth increased by 25% (29.6 mm to 36.9 mm). This moderate growth rate is attributed to the 'over-driven' state of the material: since the operating pressure ($P \geq 0.25$ MPa) already exceeds the breaking threshold ($P_{th} < 0.05$ MPa) by a factor of five, the vertical erosion process approaches a limit where further energy input yields diminishing marginal returns. Geometrically, the hole diameter remained stable in the lower pressure range before expanding by 15% at 0.55 MPa, indicating a transition where excess energy flux is diverted from vertical incision to lateral wall erosion.

Limestone (Fig. 6(b)) displayed a robust linear growth trajectory. The erosion depth extended by 53%, progressing from 15.9 to 24.3 mm. Concurrently, the hole diameter expanded from 27.6 to 33.5 mm, representing a 21% increase. Unlike sandstone, the limestone showed no saturation tendency within the tested range, suggesting that the energy input at 0.55 MPa was effectively utilized for both deepening and widening the crater in the carbonate matrix.

Granite (Fig. 6(c)) recorded the lowest absolute erosion magnitudes yet demonstrated the highest relative sensitivity to pressure variations. The hole depth surged from 11.2 to 17.9 mm, corresponding to a 60% increase. This pronounced sensitivity is physically linked to the 'threshold proximity' effect. Since the testing range (0.25–0.55 MPa) initiates precisely at the granite's breaking threshold, the material operates in the incipient failure stage. In this regime, every increment in kinetic energy decisively contributes to overcoming the inter-granular bond strength and driving crack propagation. Despite this high relative gain, the absolute depth of granite at 0.55 MPa (17.9 mm) was substantially less than that of limestone (24.3 mm), confirming that intrinsic crystalline hardness remains the primary barrier to erosion depth.

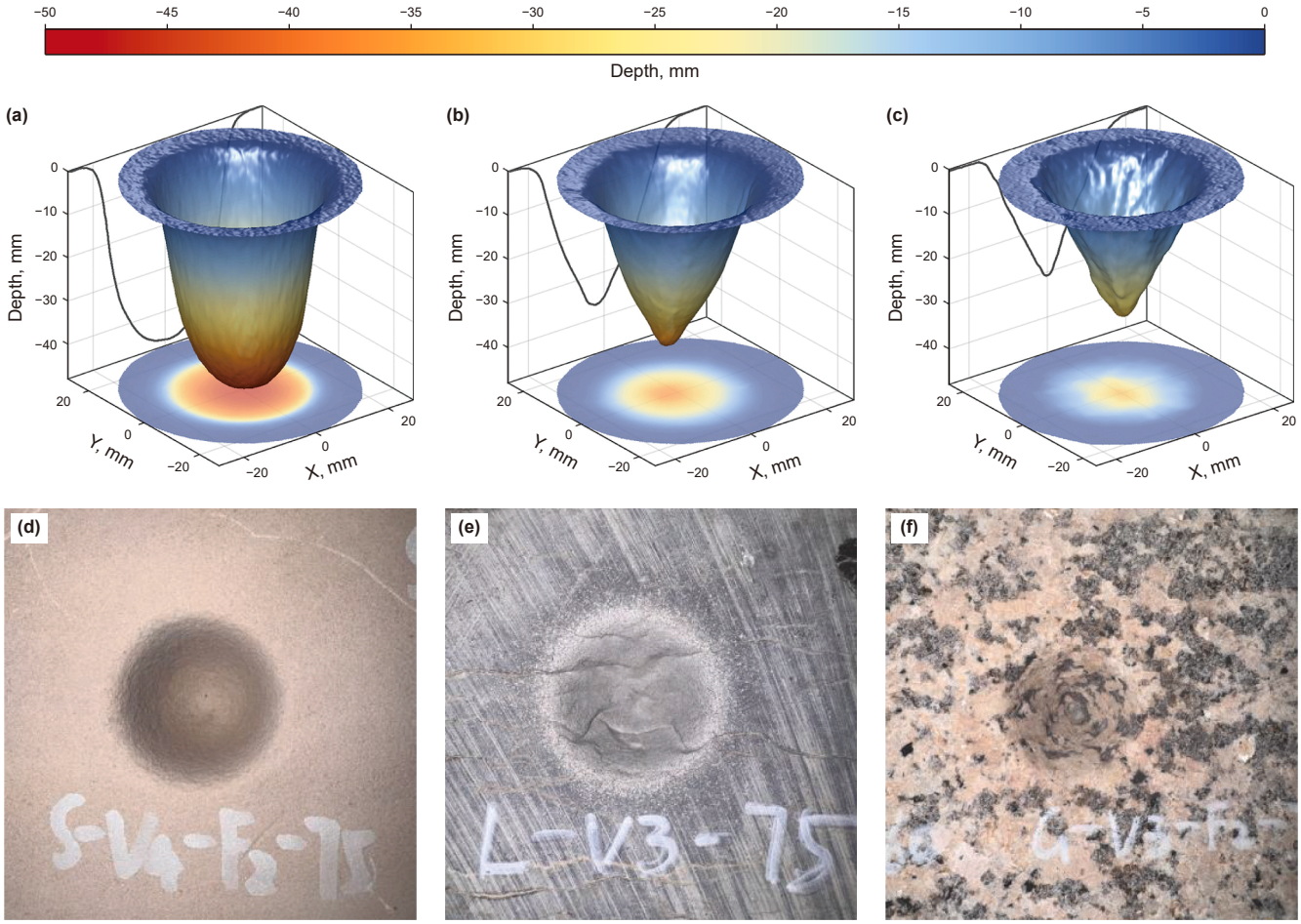


Fig. 5. Morphological comparison of erosion craters generated under a jet pressure of 0.55 MPa and exposure time of 75 s. The upper panels display 3D surface reconstructions and the lower panels show corresponding optical top-view photographs for: ((**a**), (**d**)) sandstone; ((**b**), (**e**)) limestone; and ((**c**), (**f**)) granite.

3.2.3. *Effect of exposure time on erosion dimensions*

The temporal evolution of hole depth (H_e) and average diameter (D_e) was investigated under a fixed jet pressure of 0.55 MPa, with exposure times varying from 15 to 75 s. Fig. 7 illustrates the dynamic progression of the erosion cavities. Unlike pressure, which determines the energy density threshold, exposure time governs the cumulative damage accumulation and the geometric evolution of the cavity. It is essential to clarify that the erosion limits observed are strictly dependent on the ratio between the erosion rate and the exposure duration.

Sandstone (Fig. 7(a)), being the softest lithology, completed its rapid growth phase early and exhibited a distinct global saturation characteristic. The hole depth increased from 28.1 mm at 15 s to 46.2 mm at 75 s, with a noticeable deceleration in the later stage. Concurrently, the lateral dimension reached a hydrodynamic equilibrium early; the hole diameter expanded to 41.5 mm at 45 s and subsequently plateaued. This confirms that for soft formations, the 75 s duration was sufficient to reach the aerodynamic stagnation limit, where debris accumulation prevents further dimensional expansion.

Limestone (Fig. 7(b)) demonstrated a synchronized linear growth in both dimensions. The erosion depth more than doubled from 17.2 to 37.1 mm, while the diameter expanded steadily without reaching a plateau. The absence of saturation here does not imply infinite growth potential. Instead, it indicates that due to the moderate strength of limestone, the erosion rate was steady but slower than that of sandstone, and the crater had not yet reached the critical aspect ratio required to trigger the severe debris cushioning or aerodynamic choking effects observed in the deeper sandstone cavities.

Granite (Fig. 7(c)) recorded the lowest absolute dimensions yet displayed a critical kinetic divergence between depth and diameter. While the hole depth tripled from 9.4 to 28.3 mm, the average diameter exhibited an early saturation, increasing rapidly only in the first 30 s and then stabilizing at 34.8 mm. This lateral stagnation confirms that the peripheral jet energy dropped below the granite's high breaking threshold, limiting erosion to the high-energy core zone. Crucially, despite this lateral constraint, the vertical depth at 75 s (28.3 mm) finally matched the initial depth of sandstone at 15 s (28.1 mm). This comparison confirms that the granite crater is geometrically still in the efficient shallow-hole regime. Therefore, the continuous deepening trend in Fig. 7(c) reflects that the high-strength granite requires a significantly longer exposure timeframe to reach its depth saturation limit compared to the softer lithologies.

3.2.4. *Volumetric removal characteristics*

Volumetric removal serves as a comprehensive metric for evaluating the macroscopic breakage efficiency, effectively integrating the contributions of vertical penetration and lateral expansion. Fig. 8 illustrates the evolution of erosion volume (V_e) with shaded error bands representing the experimental dispersion, superimposed with linear regression analysis to quantify the removal kinetics.

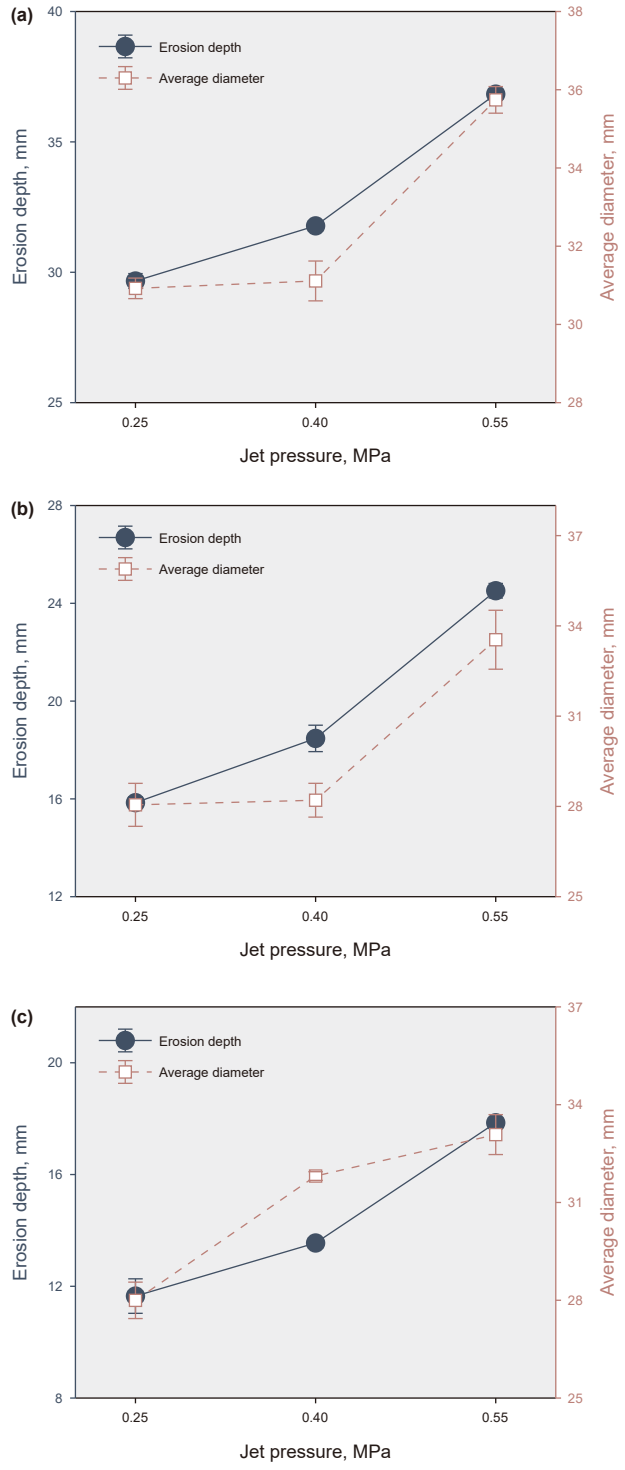


Fig. 6. Variations of erosion hole depth (H_e) and average diameter (D_e) with jet pressure under a fixed exposure time of 30 s for: (**a**) sandstone, (**b**) limestone, and (**c**) granite.

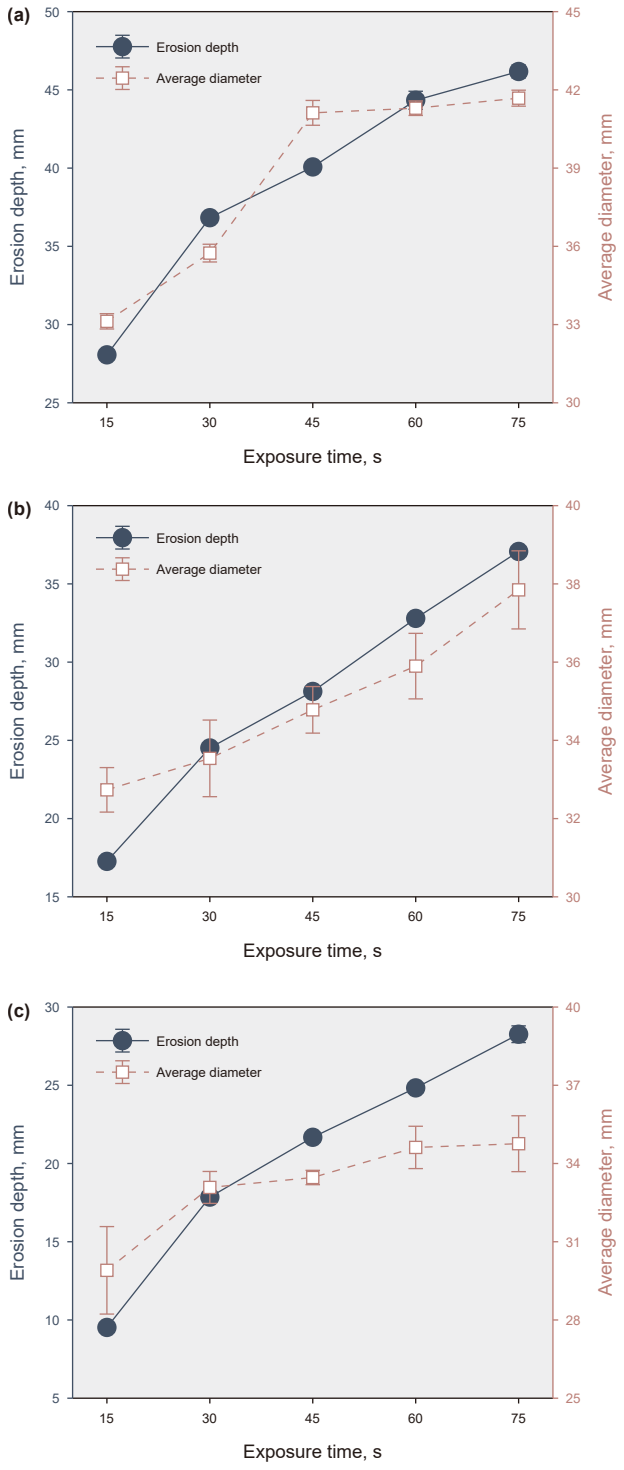


Fig. 7. Temporal evolution of erosion hole depth (H_e) and average diameter (D_e) under a fixed jet pressure of 0.55 MPa for: (**a**) sandstone, (**b**) limestone, and (**c**) granite.

A fundamental lithological segregation is immediately apparent from the pressure response (Fig. 8(a)). Sandstone exhibited the highest susceptibility to the AGJ impact, with removal volumes surging to 17170 mm^3 at 0.55 MPa, nearly triple that of the harder lithologies. This saturation coincides with the stabilization of the hole diameter observed in Section 3.2.3. To elucidate the physical cause of this attenuation, the erosion crater was photographed immediately after the jetting test (Fig. 9). The macroscopic view reveals a critical phenomenon: a layer of granular debris has stagnated at the cavity bottom. Unlike the clean sidewalls, this accumulation forms a physical barrier that separates the incoming jet from the fresh rock surface. This debris

accumulation, hereafter referred to as the 'debris cushioning effect', correlates directly with the observed volumetric saturation trend and is further analyzed in Section 4.2 (Zhang et al., 2025).

In contrast, the harder compact rocks clustered in a lower magnitude range but displayed fundamentally different kinetic behaviors. Limestone demonstrated the highest stability, maintaining a nearly perfect linear growth ($R^2 = 0.994$) throughout the 75 s duration. Granite presented a unique case. At 0.55 MPa, its erosion volume was only 10% lower than that of limestone, despite the hole depth being significantly shallower. This volumetric result suggests that substantial lateral chipping at the surface compensated for the limited vertical incision. The temporal progression of granite exhibited the lowest linearity ($R^2 = 0.908$) among the lithologies. However, unlike the asymptotic saturation seen in sandstone, this non-linearity does not stem from debris cushioning. Instead, it reflects the stochastic nature of brittle fragmentation. The volume nearly tripled between 15 s and 30 s, driven by the abrupt detachment of large, irregular chips from the sidewalls. This confirms that while granite resists deep penetration due to its high strength, the high-velocity impact sustains a robust removal process without succumbing to the premature stagnation observed in porous formations.

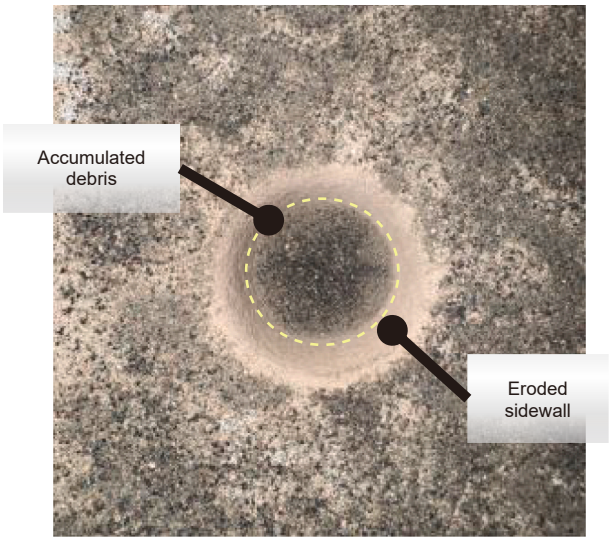


Fig. 9. Top-down view of the sandstone erosion crater ($P = 0.55$ MPa, $t = 75$ s), showing the accumulation of granular debris at the cavity bottom that induces the cushioning effect.

4. Discussion

4.1. Aerodynamic characteristics and kinetic energy transfer

To quantify the kinetic prerequisites for rock failure, the in-flight dynamics of abrasive particles were characterized using ultra-high-speed shadowgraphy. The imaging system was aligned with the optical viewports of the jetting cabinet, utilizing an i-SPEED 7 camera (iX Cameras) operating at a recording rate of 500000 fps to capture the free-jet flow field extending 250 mm downstream of the nozzle exit. Subsequent quantitative analysis was performed using high-fidelity motion tracking algorithms to extract instantaneous particle kinematics. Fig. 10 delineates the axial velocity evolution along the jet centerline derived from these measurements. Diverging from a simplified linear acceleration assumption, the velocity profiles adhere to a double-exponential association function ($R^2 > 0.85$), revealing a complex momentum transfer process governed by the varying aerodynamic drag within the expanding gas field.

Upon exiting the nozzle, the particles undergo a rapid acceleration phase driven by the high-density potential core of the gas jet, followed by a gradual stabilization phase as the slip velocity between the gas and solid phases diminishes. Crucially, at the operational standoff distance of 80 mm ($x/D^* = 10$), the particles are observed to have largely completed their acceleration stroke. This confirms that the selected standoff distance is aerodynamically optimized to harness the maximum kinetic potential of the jet before turbulent dissipation dominates the flow field.

A critical thermodynamic challenge for variable-pressure operations is the nozzle efficiency under off-design conditions. The convergent-divergent nozzle is designed for 0.55 MPa; theoretically, operating at lower pressures induces an over-expanded flow regime characterized by internal shock waves and flow separation. However, the kinematic data in Fig. 10 demonstrates the system's inertial robustness. Despite the energy penalties associated with shock structures, the solid particles act as low-pass momentum

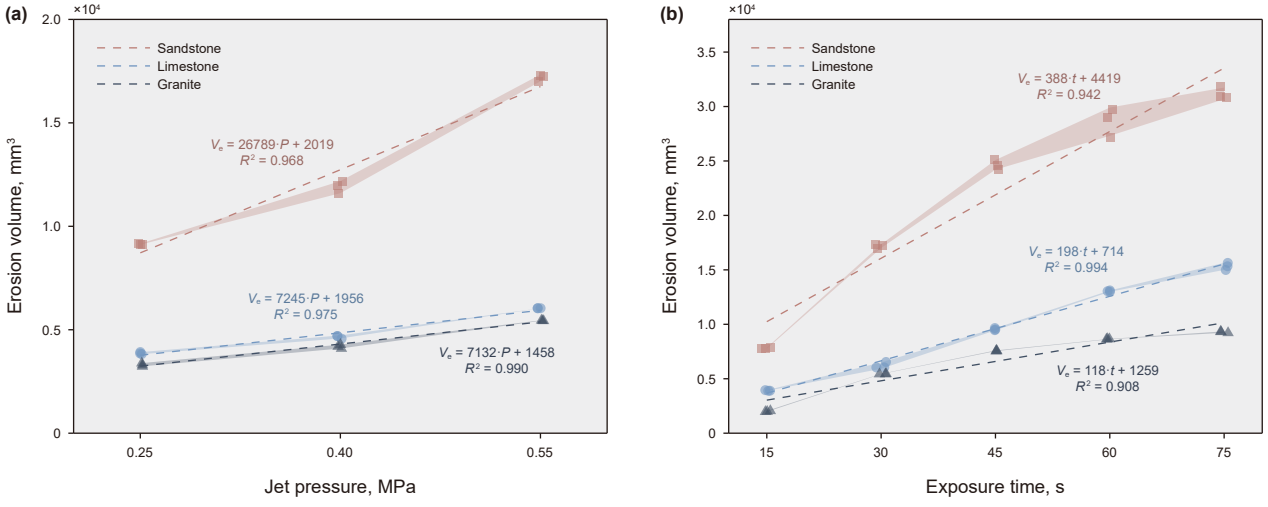


Fig. 8. Variations in volumetric removal (V_e) with (**a**) jet pressure and (**b**) exposure time for the three lithologies, superimposed with linear regression analysis to characterize the removal kinetics.

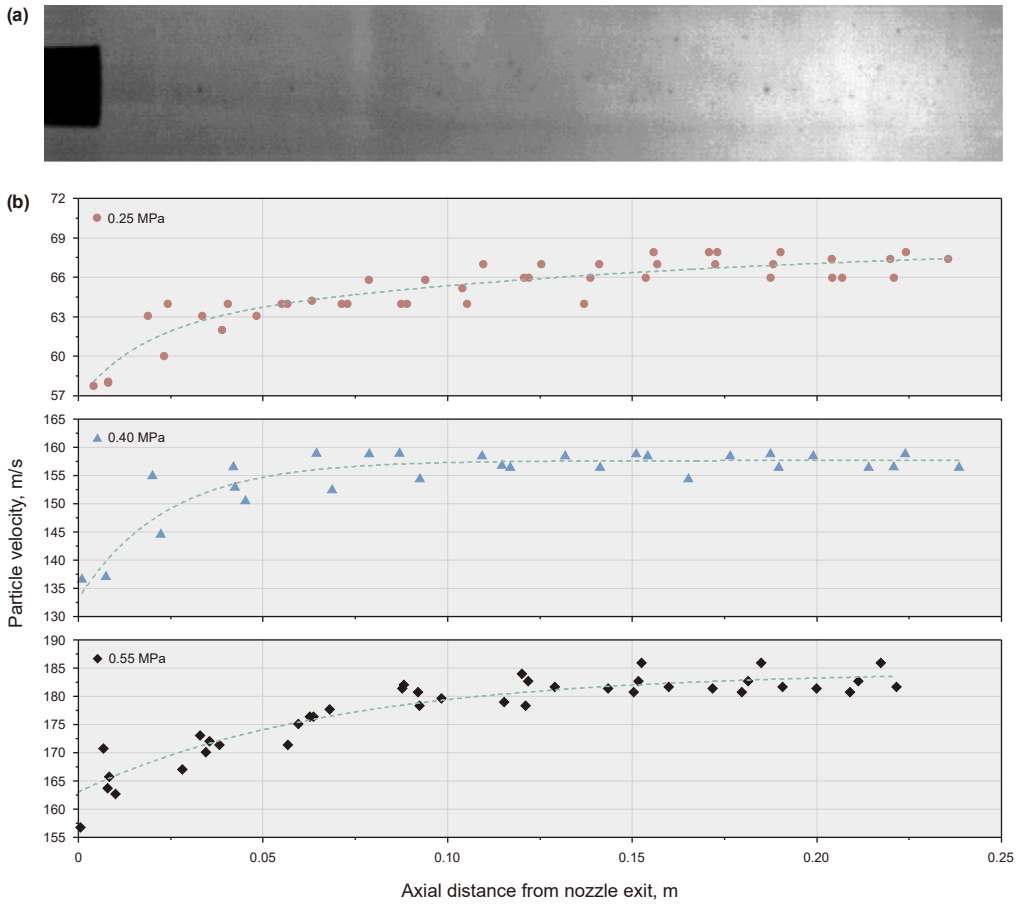


Fig. 10. Aerodynamic characteristics of the abrasive gas jet. (**a**) Representative high-speed shadowgraphy image capturing the supersonic gas-solid flow structure (at $P = 0.25$ MPa), showing a highly collimated particle stream. (**b**) Axial evolution of abrasive particle velocity along the centerline under varying driving pressures. The dashed curves represent the double-exponential fitting, revealing the rapid acceleration and subsequent inertial stabilization phases.

filters due to their significantly higher inertia relative to the gas phase. They effectively smooth out the local velocity fluctuations caused by shock boundary layer interactions. Consequently, even at the marginal pressure of 0.25 MPa, the particles successfully accumulate a terminal velocity of 67 m/s.

This aerodynamic robustness directly underpins the hole-forming capability of the system. The magnitude of the impact velocity quantified here provides the physical basis for the macroscopic erosion results observed in Section 3. These results confirm that the AGJ system delivers sufficient particle kinetic energy for rock breakage across the tested pressure range, despite the off-design compressible flow conditions within the nozzle.

4.2. Lithology-dependent failure mechanisms

The erosion tests elucidate a critical geomechanical disparity where the gas jet achieves effective rock breakage at a jet pressure of 0.25 MPa. This value is orders of magnitude lower than the uniaxial compressive strength of the target rocks, suggesting that failure is governed not by quasi-static compressive crushing but by dynamic tensile fracture. Building upon the aerodynamic data in Section 4.1, the high-velocity particle impact generates intense localized stress waves. Given that the tensile strength (σ_t) of these rocks ranges from 3.16 to 6.42 MPa and represents the weakest mechanical link, the formations are structurally vulnerable to this dynamic loading (Liu et al., 2020b). The divergence in crater morphology and kinetics reflects how different microstructures respond to this mechanism.

For the porous sandstone ($\sigma_t = 3.16$ MPa), the initial failure is driven by impact fatigue targeting the weak cementing matrix and causing rapid volumetric expansion. However, a distinct saturation trend is observed as the crater deepens. It is crucial to note that, according to the free-jet characterization in Fig. 10, the centerline particle velocity remains high within the test range. Therefore, the cessation of depth growth at 46 mm is not due to the decay of the incident jet velocity itself but rather the severe aerodynamic interference within the confined blind hole. As the crater deepens, the stratified debris architecture identified in Fig. 9 imposes a complex energy penalty. Rather than acting as a static shielding layer, the accumulated granular fines induce a regime of intense dynamic energy dissipation. The kinetic energy of the incoming high-velocity particles is largely consumed through inelastic collisions with the rebounding debris cloud and the dense fluidized bed at the crater bottom. This particle-particle interaction effectively decouples the jet momentum from the fresh rock fabric and provides the physical justification for the volumetric saturation trend quantified in Fig. 8(b).

Limestone ($\sigma_t = 4.97$ MPa) exhibits a distinct lamellar spalling failure mode governed by its sedimentary bedding planes. The impact stress waves propagate along the stratification and cause the rock to peel off in layers. This failure mode facilitates a stable erosion process. Due to its intermediate strength, the erosion rate is moderate and reaches a depth of 37 mm within 75 s. At this

depth, the return airflow remains sufficient to clear the flake-like spalled debris, and the jet velocity has not yet decayed below the failure threshold. Consequently, the system operates in a steady-state erosion regime and maintains a remarkably linear growth trajectory without exhibiting the premature stagnation typical of porous formations.

Granite ($\sigma_t = 6.42$ MPa) exhibits the highest resistance and fails primarily via brittle fracture and macroscopic chipping. The rugged V-shaped crater morphology in Fig. 5(c) reflects this chaotic crack coalescence. Regarding erosion kinetics, a divergence is observed between vertical penetration and volumetric removal. As shown in Fig. 7(c), the deepening rate decelerates in the later stages. We attribute this specifically to the geometric confinement effect in the narrow V-shaped crater where the high-velocity return airflow accelerates through the constricted annulus and creates aerodynamic resistance against the incident jet. However, it is crucial to distinguish between directional penetration and total energy efficiency. While geometric confinement hinders further vertical incision, it does not signify a cessation of the erosion process. As evidenced by the volumetric data in Fig. 8(b), the total erosion volume (V_e) of granite maintains a nearly linear growth trend ($R^2 = 0.908$) throughout the 75 s duration, without the saturation plateau seen in sandstone. This confirms that although the incident momentum is partially obstructed from reaching the crater tip, the kinetic energy is effectively redirected to fracture the sidewalls via macroscopic chipping. The coarse granite chips possess high inertia and resist the stagnation observed in fine-particle systems, allowing the AGJ system to maintain a robust volumetric removal rate despite geometric constraints.

To further quantify the sensitivity of erosion efficiency to rock mechanical properties, the total volumetric removal (V_e) at 0.55 MPa is plotted against the tensile strength (σ_t) of the target rocks in Fig. 11. Tensile strength was explicitly selected as the governing variable here to align with the stress-wave induced fracture hypothesis. The data follow an inverse exponential trend ($V_e \propto e^{-k\sigma t}$, $R^2 > 0.99$). Although only three lithologies were tested, limiting the statistical degrees of freedom, this functional form is physically consistent with the stress-wave attenuation mechanism and may serve as a preliminary predictive relationship for intermediate lithologies.

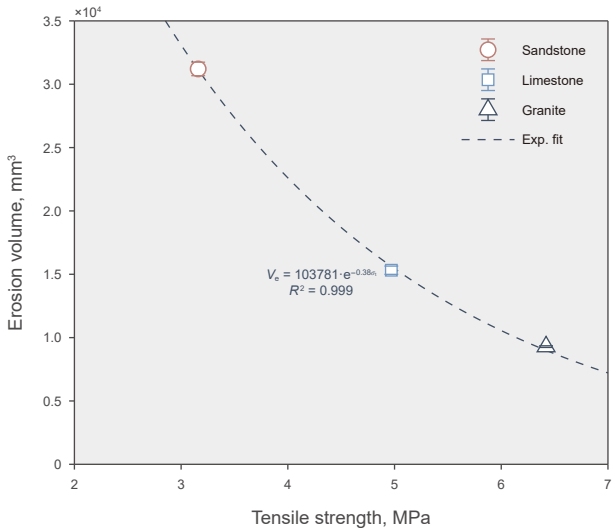


Fig. 11. Quantitative correlation between rock tensile strength (σ_t) and total erosion volume (V_e) at a jet pressure of 0.55 MPa.

4.3. Specific energy (SE) evaluation

To rigorously appraise the industrial feasibility of the AGJ system, the specific energy (SE) defined as the energy input required to remove a unit volume of rock, was adopted as the governing efficiency metric (Ahmadi et al., 2011). Unlike incompressible hydraulic jets where power is a linear product of pressure and flow rate, the energy input for the compressible gas jet is dictated by thermodynamics. Consequently, the power consumption (W) was derived based on the ideal adiabatic expansion work (Lyons et al., 2020):

$$W = \frac{k}{k-1} P_{atm} Q_{std} \left[\left(\frac{P_{abs}}{P_{atm}} \right)^{\frac{k-1}{k}} - 1 \right] \quad (2)$$

$$SE = \frac{W \cdot t}{V_e} \quad (3)$$

where $k = 1.4$ is the adiabatic index; P_{atm} is atmospheric pressure, 1.01×10^5 Pa; Q_{std} is the standard volumetric flow rate, m^3/s; and P_{abs} is the absolute jet pressure. Fig. 12 illustrates the computed SE trends. Although this calculation represents the intrinsic thermodynamic process energy and neglects mechanical transmission losses, this theoretical baseline effectively isolates the fluid dynamic efficiency from equipment-specific performance. This provides a standardized lower bound for benchmarking across technologies with disparate operational principles.

To contextualize the performance of the proposed low-pressure AGJ, the results reported by Li et al. (2023) for a swirling abrasive water jet (SAWJ) system fracturing granite of comparable strength were adopted as a benchmark. Given that the SE metric inherently normalizes for operational differences, as discussed above, a direct comparison of the thermodynamic efficiency between the two working media is warranted. Li et al. (2023) established a specific energy baseline of approximately 7.30×10^{10} J/m^3 for fracturing granite at a hydraulic pump pressure of 25 MPa. In a striking inversion, the AGJ system achieves a significantly lower SE of 4.43×10^{10} J/m^3 for the same lithology at a jet pressure of only 0.25 MPa. This data indicates that the low-pressure gas system reduces the energy cost of rock breaking by approximately 39% compared to the high-pressure hydraulic benchmark. This finding confirms that high static pressure is not an absolute prerequisite for hard rock excavation. Instead, it demonstrates that utilizing high-velocity compressible flow to accelerate abrasives offers a substantial energy cost advantage over the incompressible hydraulic pressurization method, even while operating at 1/100 th of the driving pressure.

Regarding the pressure sensitivity shown in Fig. 12(a), the results reveal that elevating the driving pressure consistently raises the energy cost per unit volume across all lithologies. Porous sandstone exhibits the lowest absolute SE of 1.59×10^{10} J/m^3 at 0.25 MPa, but this value surges by nearly 60% as pressure rises to 0.55 MPa. Since the low-pressure jet already exceeds the threshold for matrix detachment, the surplus pneumatic energy is not converted into effective erosion volume but is largely dissipated in accelerating the detached debris. Compact limestone displays an intermediate linear increase. This trend reflects a scaling disparity where the exponential rise in compressor power consumption outpaces the linear gain in material removal rate, typical for homogeneous cutting. Crystalline granite exhibits a similar monotonic increase from 4.43×10^{10} to 8.00×10^{10} J/m^3. This indicates that once the stress threshold for initiating fracture is exceeded, the marginal gain in erosion volume diminishes relative to the steep energy penalty of high-ratio compression. Consequently,

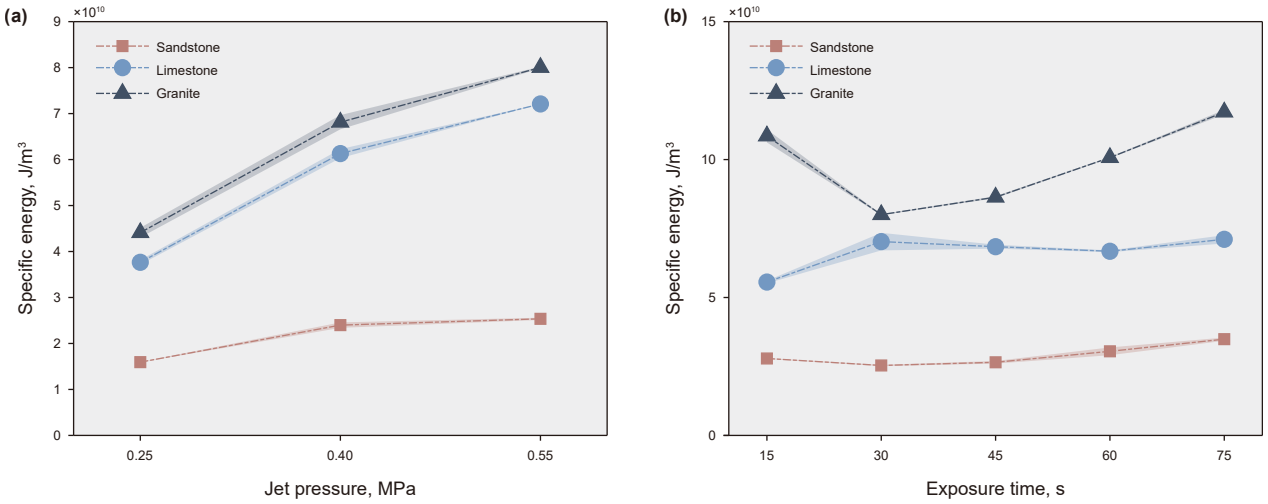


Fig. 12. Variations in specific energy (SE) with (**a**) jet pressure and (**b**) exposure time for the three lithologies.

from a strict thermodynamic perspective, the low-pressure regime represents the most efficient conversion window, although operational parameters may need adjustment to meet production rate requirements.

Temporal analysis in Fig. 12(b) elucidates the divergent energy trends rooted in rock competency. Sandstone maintains the lowest specific energy profile but exhibits a distinct upward trend after 30 s. This trajectory signifies the onset of a dynamic cushioning regime where the accumulated granular fines actively dissipate the incident kinetic energy through intense inelastic particle collisions rather than effective rock stressing. Limestone displays the most stable profile with a quasi-horizontal trajectory. This stability confirms that the debris generated by lamellar spalling is efficiently evacuated by the return airflow, thereby maintaining a steady-state energy consumption rate throughout the process. Granite, however, displays a unique non-monotonic evolution. The initial high specific energy of 10.85×10^{10} J/m^3 reflects the threshold energy barrier required to initiate damage on the pristine surface. The value reaches its minimum at 30 s as macroscopic chipping dominates the removal process but rises again in the later stages to 11.72×10^{10} J/m^3. Distinct from the collisional dissipation observed in sandstone, this late-stage energy surge in granite is attributed to the aerodynamic interference induced by geometric confinement. As the V-shaped crater deepens, the constricted return flow impedes the incident jet momentum transfer efficiency and consequently increases the energy cost per unit volume removed.

4.4. Implications for underground energy engineering

The translation of specific energy data into field protocols requires a strategic balance between energy efficiency and the rock breaking rate (RBR). The divergence in energy dissipation mechanisms observed implies that operational strategies must be tailored to the specific geological competency encountered in subsurface infrastructure projects.

For sedimentary reservoirs such as sandstone targeted for underground gas storage and carbon sequestration (Zhou et al., 2023), the operational priority is ensuring pore connectivity while minimizing energy waste. The experimental evidence of rising specific energy after 30 s confirms that continuous injection induces a cushioning phenomenon where the accumulated granular fines actively dissipate kinetic energy. Consequently, a pulsed or intermittent jetting strategy is recommended (Liu et al., 2020b). By introducing periodic purging cycles, the stagnant debris layer is cleared to reset the system to its high-efficiency state. This approach not only optimizes energy consumption but also prevents the localized compaction of debris which is vital for maintaining permeability in storage reservoirs.

In contrast, constructing access roadways or drilling into crystalline basements requires overcoming significant strength thresholds (Afolagboye et al., 2016). While this study demonstrates that granite can be broken at 0.55 MPa with high energy efficiency, the RBR at this pressure may be insufficient for time-sensitive infrastructure projects. The initiation barrier observed in the early-stage specific energy profile suggests that the impact intensity is marginal near the threshold. From an engineering perspective, prioritizing RBR over minimum specific energy is often necessary. Since standard industrial compressors deliver rated pressures up to 1.2 MPa, field operations should leverage this higher capacity. Scaling the jet pressure beyond the 0.55 MPa experimental limit is strategically justified to decisively exceed the damage initiation threshold and accelerate excavation timelines.

Finally, transferring this technology from laboratory to deep underground applications necessitates addressing the confining pressure effect. In downhole scenarios, the high ambient pressure inevitably counteracts the supersonic expansion of the gas jet which serves as the thermodynamic engine for particle acceleration. This suppression of jet expansion reduces the effective pressure ratio across the nozzle and risks stifling the particle velocity before impact. Therefore, a critical direction for future research involves quantifying the aerodynamic attenuation evolution of gas-solid flow under high-confinement regimes. Specifically, determining the critical ambient pressure threshold that triggers the transition from effective erosion to aerodynamic stagnation will be the engineering prerequisite for defining the operational depth limits of AGJ technology. Solving this fluid-dynamic bottleneck remains the most urgent challenge for translating high-efficiency gas fracturing to deep-earth realities.

5. Conclusions

This study investigated the aerodynamic kinetics and energy economy of an ultra-low-pressure abrasive gas jet (AGJ) system. The following core conclusions are drawn:

(1) The AGJ technology established critical breaking thresholds of ≤0.05 MPa (sandstone), 0.15 MPa (limestone), and 0.25 MPa (granite), verifying the feasibility of hard rock excavation without high-pressure intensification.
(2) Erosion kinetics display a fundamental lithological disparity where porous sandstone reaches a global saturation due to dynamic debris cushioning. In contrast, crystalline granite exhibits a kinetic divergence characterized by sustained vertical and volumetric growth via macroscopic chipping despite early lateral stagnation.
(3) The AGJ achieves a 39% reduction in specific energy (4.43×10^{10} J/m^3) for granite compared to hydraulic jets, while operating at only 1/100th of the driving pressure.
(4) A distinct inverse exponential correlation ($R^2 > 0.99$) was established between erosion volume and rock tensile strength. This strong non-linear dependency confirms that the AGJ breakage efficiency is fundamentally governed by the rock's tensile resistance.
(5) Operational protocols should be lithology-specific: pulsed jetting is recommended for soft formations to purge debris, whereas pressure scaling is required for hard rock to prioritize excavation speed.

CRediT authorship contribution statement

Jing-Ru Hu: Writing – review & editing, Writing – original draft, Visualization, Software, Investigation, Formal analysis, Conceptualization. **Dong Yang:** Writing – review & editing, Investigation, Data curation. **Shi-Hao Zhang:** Visualization, Investigation. **Pei-Sen Li:** Validation, Investigation. **Long-Hao Zhao:** Investigation. **Jing-Bin Li:** Supervision, Resources, Methodology. **Huan Li:** Supervision, Project administration. **Hou Zhong:** Investigation. **Zhong-Wei Huang:** Funding acquisition, Conceptualization.

Declaration of competing interest

The authors declare that they have no known competing financial interests or personal relationships that could have appeared to influence the work reported in this paper.

Acknowledgements

This work was supported by the Innovative Research Group Project of National Natural Science Foundation of China (No. 52421002) and the Science Foundation of China University of Petroleum, Beijing (No. 2462025XKBH021). This support is gratefully acknowledged by the authors, who are also grateful to the reviewers of this paper for their detailed comments.

References

Achtsnick, M., Geelhoed, P.F., Hoogstrate, A.M., et al., 2005. Modelling and evaluation of the micro abrasive blasting process. Wear 259 (1–6), 84–94. https://doi.org/10.1016/j.wear.2005.01.045.
Afolagboye, L.O., Talabi, A.O., Akinola, O.O., 2016. Evaluation of selected basement complex rocks from Ado-Ekiti, SW Nigeria, as source of road construction aggregates. Bull. Eng. Geol. Environ. 75 (2), 853–865. https://doi.org/10.1007/s10064-015-0766-1.
Ahmadi, M., Erfan, M.R., Torkamany, M.J., et al., 2011. The effect of interaction time and saturation of rock on specific energy in ND: YAG laser perforating. Opt. Laser Technol. 43 (1), 226–231. https://doi.org/10.1016/j.optlastec.2010.06.018.
Ait Baha, A., Amri, I., Ouabid, M., et al., 2025. Petrographic, physical–mechanical and fracture modeling of granites: An integrated approach to evaluating the stone reserves and mineral deposits of Ment Granite (western Meseta, Central Massif of Morocco). Bull. Eng. Geol. Environ. 84 (5), 252. https://doi.org/10.1007/s10064-025-04278-z.
Cox, E.P., 1927. A method of assigning numerical and percentage values to the degree of roundness of sand grains. J. Paleontol. 1 (3), 179–183.
Deng, L., Zhang, C., Zhuang, Q., et al., 2022. Development and application of a full-scale mechanical rock-cutting platform for measuring the cutting performance of TBM cutter. Measurement 204, 112036. https://doi.org/10.1016/j.measurement.2022.112036.
Ehlig-Economides, C.A., 2023. Geologic carbon dioxide sequestration methods, opportunities, and impacts. Curr. Opin. Chem. Eng. 42, 100957. https://doi.org/10.1016/j.coche.2023.100957.
Fu, X., Xiong, C., Shi, H., et al., 2025. Comparative analysis of rock breakage characteristics and failure mode on conventional and conical PDC cutter cutting carbonate. Pet. Sci. 22 (2), 821–834. https://doi.org/10.1016/j.petsci.2024.12.016.
Gao, M.Z., Yang, B.G., Xie, J., et al., 2022. The mechanism of microwave rock breaking and its potential application to rock-breaking technology in drilling. Pet. Sci. 19 (3), 1110–1124. https://doi.org/10.1016/j.petsci.2021.12.031.
Ge, Z., Zhang, H., Zhou, Z., et al., 2023. Experimental study on the characteristics and mechanism of high-pressure water jet fracturing in high-temperature hard rocks. Energy 270, 126848. https://doi.org/10.1016/j.energy.2023.126848.
Hamzaban, M.T., Rostami, J., Dahl, F., et al., 2023. Wear of cutting tools in hard rock excavation process: A critical review of rock abrasiveness testing methods. Rock Mech. Rock Eng. 56 (3), 1843–1882. https://doi.org/10.1007/s00603-022-03187-x.
He, Z., Li, G., Tian, S., et al., 2016. SEM analysis on rock failure mechanism by supercritical CO_2 jet impingement. J. Pet. Sci. Eng. 146, 111–120. https://doi.org/10.1016/j.petrol.2016.04.023.
Hong, C., Yang, R., Huang, Z., et al., 2021. Experimental investigation on coal-breakage performances by abrasive nitrogen-gas jet with a conical nozzle. Int. J. Rock Mech. Min. Sci. 142, 104781. https://doi.org/10.1016/j.ijrmms.2021.104781.
Hu, J., Huang, Z., Wu, S., et al., 2025. Numerical investigation of flow field characteristics and key structural parameters impact in ice air jet based on Laval nozzle. Powder Technol. 455, 120768. https://doi.org/10.1016/j.powtec.2025.120768.
Hu, Y., Zhang, J., Han, R., et al., 2026. Optimization of geometry parameters for a high-performance supersonic abrasive jet nozzle: An experimental and numerical study. Vacuum 243, 114831. https://doi.org/10.1016/j.vacuum.2025.114831.
Huang, M., Hu, Y., Wang, X., et al., 2020. Experimental investigation on the flow and rock breaking characteristics of supercritical carbon dioxide jets. J. Pet. Sci. Eng. 187, 106735. https://doi.org/10.1016/j.petrol.2019.106735.
Huang, W., Lu, S., Hersi, O.S., et al., 2017. Reservoir spaces in tight sandstones: Classification, fractal characters, and heterogeneity. J. Nat. Gas Sci. Eng. 46, 80–92. https://doi.org/10.1016/j.jngse.2017.07.006.
Joo, G.W., Oh, T.M., Hwang, H.J., et al., 2023. Evaluating the efficacy of recycled garnet abrasives in enhancing hard rock cutting performance of abrasive waterjet systems. Int. J. Rock Mech. Min. Sci. 167, 105407. https://doi.org/10.1016/j.ijrmms.2023.105407.
Li, G., Wu, X., Song, X., et al., 2022. Status and challenges of hot dry rock geothermal resource exploitation. Pet. Sci. Bull. 7, 343–364. https://doi.org/10.3969/j.issn.2096-1693.2022.03.031 (in Chinese).
Li, H., Huang, Z., Li, J., et al., 2023. Performances of different abrasive materials during swirling impeller abrasive water jet drilling of granite. Rock Mech. Rock Eng. 56 (6), 4343–4361. https://doi.org/10.1007/s00603-023-03222-5.
Li, H., Li, J., Huang, Z., et al., 2025a. Numerical investigation of abrasive water jet rock damage characteristics that considers the shape, the interaction and the fragmentation of abrasive particles. Rock Mech. Rock Eng. 58 (2), 2105–2131. https://doi.org/10.1007/s00603-024-04297-4.
Li, S., Jiao, B., Deng, B., et al., 2025b. Impact of water–rock interaction on microstructure damage of carbonate rocks and alteration of its micromechanical properties. Phys. Fluids 37, 077104. https://doi.org/10.1063/5.0265540.
Liu, W., Zhang, Z., Fan, J., et al., 2020a. Research on gas leakage and collapse in the cavern roof of underground natural gas storage in thinly bedded salt rocks. J. Energy Storage 31, 101669. https://doi.org/10.1016/j.est.2020.101669.
Liu, Y., Cui, J., Xu, Z., et al., 2020b. Comparison of the rock breakage pressure of abrasive water jets and abrasive air jets. Geomech. Geophys. Geo-Energy Geo-Resour. 6, 27. https://doi.org/10.1007/s40948-020-00150-4.
Liu, Y., Liang, B., Liu, X., 2017. Experimental and numerical optimization of coal breakage performance parameters through abrasive gas jet. Int. J. Heat Technol. 35, 747–754. https://doi.org/10.18280/ijht.350408.
Liu, Y., Zhang, J., Wei, J., et al., 2020c. Optimum structure of a laval nozzle for an abrasive air jet based on nozzle pressure ratio. Powder Technol. 364, 343–362. https://doi.org/10.1016/j.powtec.2020.01.086.
Liu, Y., Zhang, J., Zhang, T., et al., 2018. Optimal nozzle structure for an abrasive gas jet for rock breakage. Geofluids 2018, 9457178. https://doi.org/10.1155/2018/9457178.
Lu, Y., Xiao, S., Ge, Z., et al., 2019. Experimental study on rock-breaking performance of water jets generated by self-rotatory bit and rock failure mechanism. Powder Technol. 346, 203–216. https://doi.org/10.1016/j.powtec.2019.01.078.

Lyons, W.C., Stanley, J.H., Sinisterra, F.J., et al., 2020. Air and gas drilling manual: Applications for oil, gas, geothermal fluid recovery wells, specialized construction boreholes, and the history and advent of the directional DTH. Elsevier.

Porcarelli, S., Shedde, D., Wang, Z., et al., 2021. Tension and shear anchorage systems for limestone structures. Constr. Build. Mater. 272, 121616. https://doi.org/10.1016/j.conbuildmat.2020.121616.

Ranjith, P.G., Liu, Y., Wei, J., et al., 2019. Effect of abrasive mass flow on the abrasive acceleration and erosion rates of abrasive gas jets. Rock Mech. Rock Eng. 52, 3085–3102. https://doi.org/10.1007/s00603-019-01746-3.

Ren, J., Wu, Y., Mao, X., et al., 2025. Sensitivity of three-dimensional boundary layer stability to intrinsic uncertainties of fluid properties: A study on supercritical CO_2. J. Fluid Mech. 1007, A7. https://doi.org/10.1017/jfm.2025.100.

Song, J., Zhang, D., 2013. Comprehensive review of caprock-sealing mechanisms for geologic carbon sequestration. Environ. Sci. Technol. 47 (1), 9–22. https://doi.org/10.1021/es301610p.

Sun, Z., Mu, Z., Huang, Z., et al., 2024. Hard rock drilling characteristics under axial-torsional isofrequency impact: Insights for improving efficiency of deep energy mineral excavation. Geoenergy Sci. Eng. 240, 213089. https://doi.org/10.1016/j.geoen.2024.213089.

Ulusay, R. (Ed.), 2015. The ISRM suggested methods for rock characterization, testing and monitoring: 2007-2014. Springer International Publishing.

Wang, H., Li, G., He, Z., et al., 2018. Experimental investigation on abrasive supercritical CO_2 jet perforation. J. CO2 Util. 28, 59–65. https://doi.org/10.1016/j.jcou.2018.09.018.

Wang, H., Li, G., Shen, Z., et al., 2015. Experiment on rock breaking with supercritical carbon dioxide jet. J. Pet. Sci. Eng. 127, 305–310. https://doi.org/10.1016/j.petrol.2015.01.006.

Wang, H., Liao, H., Wei, J., et al., 2023. Stress release mechanism of deep bottom hole rock by ultra-high-pressure water jet slotting. Pet. Sci. 20 (3), 1828–1842. https://doi.org/10.1016/j.petsci.2022.12.002.

Wei, J., Cai, Y., Zhang, T., et al., 2025. An evaluation model and its application of low-pressure abrasive air jet slitting hard rock. J. China Coal Soc. 50, 349–359. https://doi.org/10.13225/j.cnki.jccs.YG24.1425 (in Chinese).

Xi, W., Yang, D., Skripov, P., et al., 2025. Quantitative experiment and numerical simulation on sub-critical and supercritical CO_2-N_2 multiphase jet flows. Int. J. Heat Fluid Flow 114, 109830. https://doi.org/10.1016/j.ijheatfluidflow.2025.109830.

Zhang, H., Liu, X., Wei, J., et al., 2025. Rock breakage mechanisms in TBM disc cutters cutting with abrasive air jet grooving: Effects of groove depth and spacing. Geotech. Geol. Eng. 43 (7), 354. https://doi.org/10.1007/s10706-025-03331-8.

Zhang, Y., Zhao, G.F., 2019. A global review of deep geothermal energy exploration: From a view of rock mechanics and engineering. Geomech. Geophys. Geo Energy Geo Resour. 6 (1), 4. https://doi.org/10.1007/s40948-019-00126-z.

Zhao, Y., Yang, H., Chen, Z., et al., 2019. Effects of jointed rock mass and mixed ground conditions on the cutting efficiency and cutter wear of tunnel boring machine. Rock Mech. Rock Eng. 52 (5), 1303–1313. https://doi.org/10.1007/s00603-018-1667-y.

Zhou, J., Deng, G., Tian, S., et al., 2023. Experimental study on the permeability variation of sandstone at cyclic stress: Implication for underground gas storage. J. Energy Storage 60, 106677. https://doi.org/10.1016/j.est.2023.106677.